Journal of
Materials Chemistry A

PAPER

View Article Online
View Journal | View Issue

Cite this: *J. Mater. Chem. A*, 2024, **12**, 6652

Insights into the active nickel centers embedded in graphitic carbon nitride for the oxygen evolution reaction†

Nicolò Rossetti,[a] Aldo Ugolotti,[b] Claudio Cometto,[a] Verónica Celorrio,[c] Goran Dražić,[d] Cristiana Di Valentin*[b] and Laura Calvillo*[a]

Received 29th November 2023
Accepted 5th February 2024

DOI: 10.1039/d3ta07389k

rsc.li/materials-a

Experimental and theoretical studies have demonstrated that the use of single atom catalysts (SACs) for energy conversion processes is very promising. However, their stability under catalytic conditions is the main issue that hinders their commercial use. In this work, we report an oxygen evolution catalyst based on single nickel atoms stabilized in triazine-based carbon nitride (CN) and a detailed study of the evolution of the Ni centers under catalytic conditions. The nanostructured materials have been characterized by combining experimental techniques, such as X-ray diffraction, transmission electron microscopy, X-ray absorption and X-ray photoemission spectroscopy, with DFT theoretical calculations to determine the CN structure, the metal adsorption sites, the coordination of the Ni atoms, and the changes undergone under catalytic conditions. Electrochemical characterization showed a linear increase of the catalytic activity with Ni loading. The stability of the materials was studied by HR-TEM and XAS post-catalysis measurements and DFT simulations. Results indicated a partial chemical restructuring of the single Ni atoms under catalytic conditions with the formation of Ni–O–Ni moieties, stabilized in the CN cavities, which are the real catalytic species.

1 Introduction

The depletion of fossil fuels and the increase of atmospheric CO_2 levels are encouraging the continuous search for alternative energy sources. This change of our energy system involves an increase of storage and interplay of different renewable energy sources, which can be used for driving important energy conversion reactions.[1–3] In this new energetic framework, the production of hydrogen from water in electrolysers using renewable energy, without emitting CO_2, will be of key importance for the transition to a sustainable mobility system and the basis for a decarbonised economy.[4]

Among the different types of electrolysers, those working with alkaline electrolytes (alkaline water electrolyser, AWE) are particularly promising due to their mature and robust technology.[5] In addition, the nature of such electrolytes allows the use of non-noble metal-based catalysts, which can help to dramatically reduce the costs and increase the efficiency of the electrochemical devices. In this perspective, the scientific community is making huge efforts to develop low cost, highly active and stable non-noble metal catalysts for both the hydrogen and oxygen evolution reactions. The development of an optimal catalyst for the oxygen evolution reaction (OER) is particularly challenging due to its slow kinetics and the harsh working conditions.[6] Transition metals (TMs), especially 3d metals, are the best option as OER catalysts due to their high abundance, affordable price, and high catalytic activity.[7] Among them, nickel is predicted to be the most efficient one.[8–10]

From the materials science point of view, many efforts have been made in order to improve the performance of TM-based catalysts by modifying their morphology, structure and size, since a strong dependence on their physical form has been reported.[11] Very interesting properties have been observed by gradually decreasing the size from bulk materials to nanoparticles (NPs) and to single atoms.[12] The atomic-scale size exhibits unique characteristics, which are governed by quantum size effects, where confinement of electrons leads to a discrete energy level distribution.[13,14] The dispersion of single metal atoms in the support, usually called single atom catalysts (SACs), allows a maximization of the atomic efficiency (100%) of the metal catalyst, which often show outstanding performance in terms of specific activity and selectivity.[11] Unfortunately,

---

[a] *Dipartimento di Scienze Chimiche, Università di Padova and INSTM Research Unit, Via Marzolo 1, 35131 Padova, Italy. E-mail: laura.calvillolamana@unipd.it*

[b] *Department of Materials Science, Università degli Studi di Milano-Bicocca, Via Cozzi 55, 20125 Milano, Italy. E-mail: cristiana.divalentin@unimib.it*

[c] *Diamond Light Source Ltd, Diamond House, Harwell Science and Innovation Campus, Didcot, Oxfordshire OX11 0DE, UK*

[d] *Department of Materials Chemistry, National Institute of Chemistry, Hajdrihova 19, SI-1000 Ljubljana, Slovenia*

† Electronic supplementary information (ESI) available: Description of the numerical screening of both pristine and Ni-decorated CN models, and additional experimental (structural, elemental, spectroscopic and electrochemical) characterization. See DOI: **https://doi.org/10.1039/d3ta07389k**

SACs are often unstable and tend to aggregate into clusters or NPs because of the high surface energy of the atomically dispersed metal atoms, which enhances their mobility on the support surface.[14,15] Under catalytic conditions this effect is even more severe, since the interaction between the single atoms and the substrate decreases due to new interactions established between the metal atoms and the reactant, lowering the migration barrier of single metal atoms and favouring their agglomeration into small clusters. Long-term stability is crucial for the applicability of SACs in technological applications. Catalysts based on single metal atoms are sensitive to agglomeration and/or leaching out.[16–20] Additionally, the support might also degrade during long-term application under harsh OER operating conditions. In order to improve the stability of the catalyst, the support has to be able to strongly stabilize the metal atoms avoiding their agglomeration. The stabilization can be mainly reached by following two strategies: (i) the establishment of strong metal-support interactions, and/or (ii) the confinement of the single atoms into a limited space, thus decreasing their mobility.[21–24]

The state of the art of OER catalysts based on SACs mainly consists of TM atoms dispersed in a substrate and stabilized through heteroatoms.[25–30] The most commonly used heteroatom is nitrogen, while Co, Ni and Fe are the most used metals due to their electronic configuration (vacant orbitals and d electrons). However, even though density functional theory (DFT) predictions have identified SACs as one of the most efficient OER electrocatalysts,[26,31–33] experimental evaluations have not been widely reported for OER activity due to the complex synthesis methods and the unstable coordination under catalytic conditions.

In this work, we have used a triazine-based carbon nitride as a substrate to stabilize Ni single atoms. Carbon nitride (CN) is a polymeric organic semiconductor that consists of 2D layered structures that can be easily synthesized from several precursors, such as melamine, urea, thiourea, *etc.*[34,35] and shows high physicochemical stability and non-toxicity. It presents structural cavities (three-, six-, or nine-fold N cavities, depending on the polymorph) where SACs could be confined and stabilized through strong metal–nitrogen interactions.[36,37] In addition, CN contains a higher amount and uniform type/arrangement of nitrogen species, compared with the commonly used nitrogen-doped carbon materials, thus offering abundant and more-precisely-defined coordination sites for single atoms than N-doped carbon systems.[38–41] The prepared catalysts have been characterized by a large variety of techniques in order to gain a comprehensive understanding of their physicochemical properties. The experimental observations have been combined with DFT simulations of several models of CN and of their XPS spectra to achieve an atomistic description of the systems under investigation. Materials with different Ni loadings have been tested as OER catalysts. Finally, the stability of this type of material has been evaluated after the electrochemical work to determine any possible structural change or formation of new active species, and to prove that CN is able to stabilize the Ni atoms thanks to the strong nickel–nitrogen interaction and the confinement in its structural cavities.

2 Results and discussion

2.1 Morphological and structural characterization

2.1.1 Pristine CN. A triazine-based graphitic carbon nitride (CN) heterostructure was obtained by co-polymerization of cyanuric chloride and melamine in solution at low temperature. In this section, the characterization of the CN substrate is discussed, presenting the details of the atomic structure before the insertion of Ni atoms. With this aim, we performed a combined experimental and theoretical investigation based on structural and spectroscopic techniques, *i.e.* transmission electron microscopy (TEM), X-ray diffraction (XRD) and X-ray photoemission spectroscopy (XPS), and on DFT calculations. The detailed description of the numerical techniques is reported in Section 3.4. Different geometries were tested by DFT, considering different polymerization degrees, *i.e.* full or partial polymerization of melamine monomers and full polymerization of condensed molecules, as well as different arrangements of the monomers. However, only the configuration presenting the best agreement with the experimental data is discussed in the next sections. The detailed computational study of the other structures is reported in the ESI (see Fig. S1†).

The low-temperature method of synthesis used in this work allowed the control of the polymerization process, resulting in a layered-like structure with nanosheets of some hundreds of nanometers, as observed by TEM in Fig. 1a and S2.† Usually, the CN sheets are obtained in two steps through the exfoliation of the bulk material prepared at high temperature (500–600 °C).[42–45] Our method, in contrast, allows CN thin sheets to be obtained in only one step and at low temperature, without the need for an exfoliation treatment.

In order to obtain atomistic information on the actual structure of the CN substrate, the experimental XRD pattern was compared with that simulated from DFT models, as reported in Fig. 1b. The experimental XRD pattern shows two diffraction peaks at 27.6° and 10.6°, indexed to the (001) and (110) planes of CN, respectively. The first peak is characteristic of the interlayer stacking of the conjugated aromatic systems and corresponds to an interlayer distance of 0.33 nm, which is in agreement with the values reported in the literature for this kind of material.[37,46,47] The second peak corresponds to an intralayer distance of 0.71 nm, which is associated with the in-plane distance between repeated units. Based on this last peak, some considerations can be made on the details of the CN structure. The tris-*s*-triazine (or heptazine) and the *s*-triazine-based structures of CN show the (100) peak at 13.1° and 17.4°, respectively.[48,49] Therefore, these structures can be excluded for our CN material. The peak at 10.6° fits better with a hexagonal crystal structure already reported in the literature.[37,46] Among all the optimized DFT CN structures considered for this study (reported in Fig. S1g†), that reported in Fig. 1e is the one whose calculated parameters better fit with the experimental data. For this model, two XRD peaks were obtained by our calculations, one at 25.7°, corresponding to the stacking distance of the heterostructure of 0.35 nm, and the other at ~11.2°, which corresponds to the superposition of the

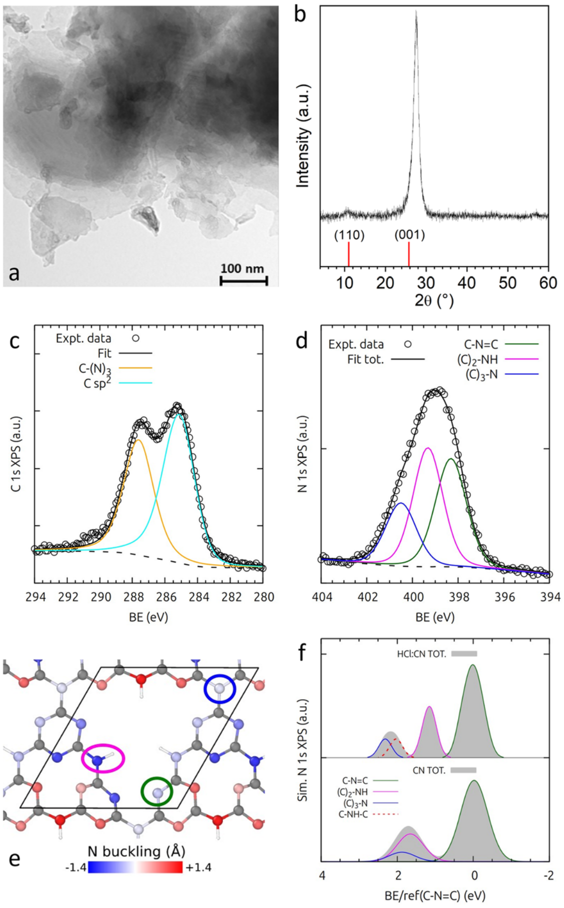

Fig. 1 Characterization of the pristine CN substrate: (a) representative TEM image; (b) experimental (black line) and simulated (red sticks) XRD patterns; experimental (c) C 1s and (d) N 1s XPS data; (e) optimized 2D DFT structure; (f) simulated N 1s XPS spectra. In panel (e), C and H atoms are represented by grey and white spheres, while N atoms are colored using their relative height difference. The black line shows the structure of the computational cell.

diffraction from the (100), (010), and (110) planes of the primitive cell, with distances of 0.78 nm, 0.81 nm and 0.79 nm, respectively. Based on this combined experimental/computational analysis, we can conclude that the CN substrate is constituted by a hexagonal arrangement of triazine-based monomers, with small and large cavities.[42]

XPS measurements were performed to determine the types of carbon and nitrogen species present in the material. Regarding the C 1s region (Fig. 1c), CN shows the component at 287.8 eV, which is attributed to C–(N)$_3$ and is characteristic of CN materials.[50–52] The C 1s component at 285.0 eV can be related to the adventitious carbon present in the sample holder, which is visible due to the very thin film of sample deposited in order to avoid charging effects,[52] and/or a small residue of pyridine trapped in the CN structure.

The N 1s region, however, gives more information about the CN structure. Therefore, it was studied in more detail. The comparison of the experimental XPS spectra with the simulated one is reported in Fig. 1d and f. The broad experimental N 1s region can be separated into three features at binding energies (BEs) of 398.5 eV, 399.5 eV, and 400.5 eV, associated with pyridinic N, amino (C$_2$–NH) species, and the overlap of protonated pyridinic N (–NH species) with graphitic N species ((C)$_3$–N species), respectively (Fig. 1d).[50–53] This assignment of the N 1s components is supported by our DFT calculations, which can predict the relative energy shift from the peak with the lowest BE. Interestingly, models of two-dimensional layers obtained through different degrees of condensation of the melamine precursors resulted in similar spectra, which presented only two components separated by 1.6–2.0 eV (Fig. S1h†). The peak at the lowest BE is attributed to pyridinic N atoms, whereas the one at the highest BE is the result of the photoemission from both graphitic and amino N atoms. The experimental peak at 399.5 eV can be effectively simulated assuming the presence of residual hydrogen chloride from the synthesis, whose presence was confirmed by XPS (Fig. S4a†). Chlorine ions come from the formation of HCl as a by-product of the chemical condensation between melamine and cyanuric chloride and has been observed in the literature for a similar synthesis.[46] Then, the additional component originates from the adsorption of protons coming from HCl by pyridinic N atoms (the structure with H$^+$ and Cl$^-$ ions included within the CN layer is shown in Fig. S1f†), which causes a redshift of the photoemission from the amino N component by ~0.5 eV. However, the additional atoms do not induce major perturbations in the crystal structure of CN.

2.1.2 Nickel-decorated CN.

Having defined the most probable structure of the CN substrate, in this section we present the characterization results for the Ni-modified CN samples with different Ni loadings, labelled as Ni–CN(*X*), with *X* being the nominal molar Ni : CN ratio.

TEM images showed that the introduction of nickel in the CN matrix did not cause morphological changes in the material, as deduced from the comparison of Fig. 1a and 2a. It must be highlighted that no nanoparticles were observed, excluding their formation during the metalation process. High-resolution TEM-EDXS analysis confirmed the presence of single Ni atoms only, which are clearly observed in Fig. 2b and c as dark and bright dots, respectively. HRTEM images suggested that no subnanometer clusters were formed in the sample. The homogeneous dispersion of C, N, and Ni elements in Ni–CN was further verified by EDX analysis (Fig. 2d–h). The XRD patterns of the Ni–CN samples, reported in Fig. 3a, only show the two characteristic peaks of the CN substrate. The absence of secondary peaks related to Ni phases (metal, (hydr)oxides, carbides or nitrides expected in the region between 35° and 60°)[54–56] also confirms the absence of Ni-based nanoparticles larger than 2 nm.

To clarify the structure of the Ni–CN samples, we introduced a NiCl$_2$ unit in the structure of Fig. 1e resulting in two models (presented and discussed in detail in Fig. S6† with reference to the adsorption energy). We did not observe any substantial difference in the XRD patterns of CN samples with and without the inclusion of Ni atoms. Our choice to introduce one single Ni atom per supercell is supported by the experimental TEM images where no Ni clusters were identified. In the following, we will further characterize and discuss only the model with the strongest binding to the adatom, shown in Fig. 3c (also reported

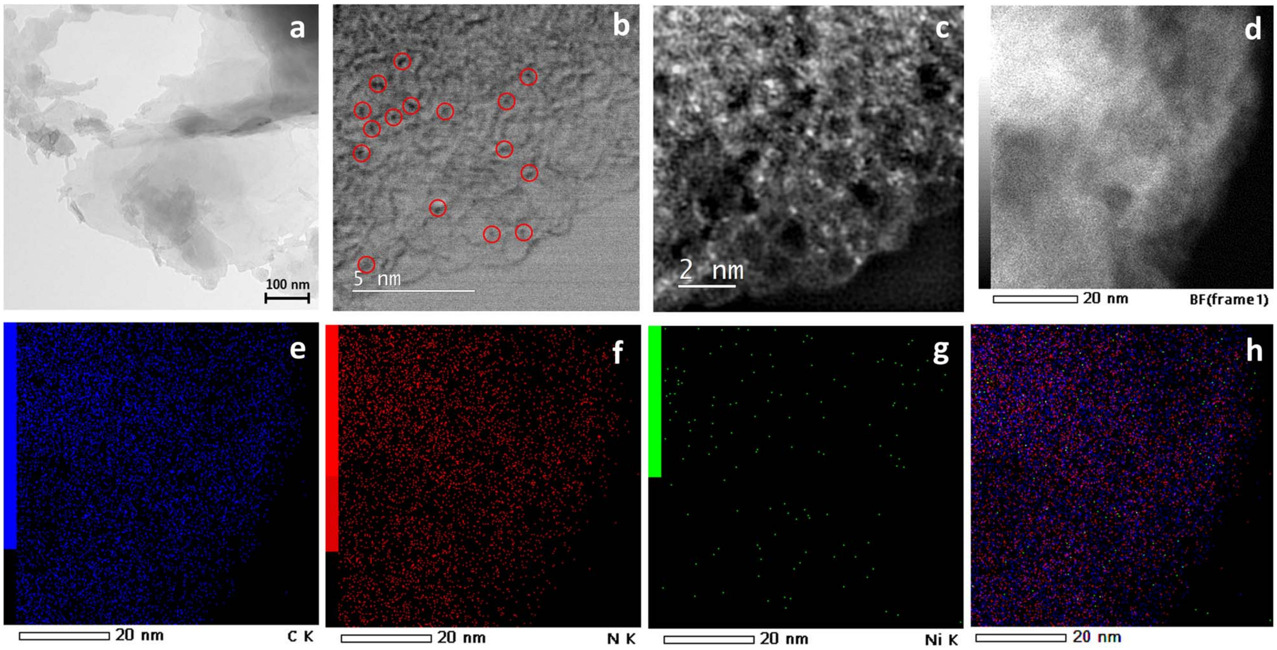

Fig. 2 Morphological characterization of Ni–CN(0.2): (a) representative TEM image; (b) BF-STEM and (c) HAADF-STEM images; (d) DF-STEM image; and (e)–(h) corresponding elemental mapping images of C, N, and Ni, and their overlapping. The single Ni atoms are represented as dark dots in (b), where some of them are indicated with red circles, and bright dots in (c).

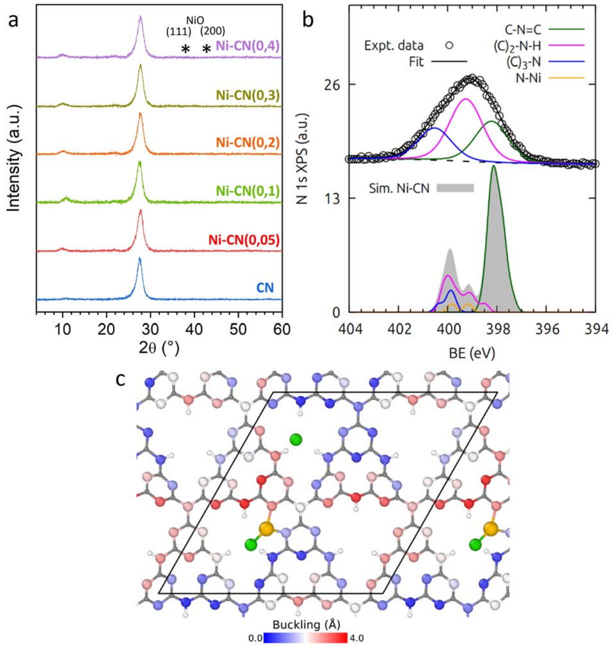

Fig. 3 Structural characterization of Ni–CN: (a) XRD patterns of CN and Ni–CN(*X*) samples; (b) experimental and calculated N 1s XPS region for Ni–CN(0.2), and the corresponding deconvolution into chemically shifted components; and (c) proposed structure for Ni–CN samples determined from the combination of experimental results and DFT calculations where a $NiCl_2$ unit was inserted in the CN model. In panel (c), the C, H, Cl, and Ni atoms are represented by grey, white, green, and orange spheres, respectively, while N atoms are colored by their relative height difference. The black line shows the structure of the computational cell.

in Fig. S6b†). Here, Ni binds to two pyridinic N atoms at the edge of the large cavity and is also coordinated by a Cl^- ion (the other Cl^- ion is in another cavity of the same size). The planar coordination of Ni atoms with two (or more) pyridinic N atoms has already been proposed in the literature for single metal atoms embedded in CN substrates.[57–59]

The location and the coordination sites of the Ni atoms were experimentally investigated by XPS. Fig. 3b shows the analysis of the experimental N 1s XPS region after the addition of Ni atoms. This region can be fitted again with three components at (i) 398.3 eV, (ii) 399.2 eV and (iii) 400.3 eV. Based on the discussion for the CN substrate, we assigned these peaks to (i) pyridinic N, (ii) amino N (after the protonation of pyridinic N atoms in the same cavity), and (iii) residual amino N (from those cavities without the additional proton) overlapping with graphitic N species, respectively. In comparison with the pristine CN, a shift of 0.2 eV and 0.3 eV toward lower BE values was observed for the pyridinic N and –NH components, respectively. This effect can be directly related to the interaction of Ni atoms with the N species of the substrate and agrees with the electronic transfer from Ni centres to N species, due to the lower electronegativity of the Ni atom. The calculated XPS spectrum, reported in Fig. 3b, presents three peaks (in grey) whose number and energy separation are in agreement with those obtained after deconvolution of the experimental spectrum. In particular, this comparison allows us to identify a contribution to the central component at intermediate BE (*c.a.* 399 eV) from the N species interacting with Ni (in orange).

In our model in Fig. 3c, for simplicity, the Ni–CN structure does not include any additional protons and chlorine ions, which, in contrast, we have proved to be residual after the CN synthesis step and/or the metalation step. Therefore, one should consider the contribution of this species to the XPS spectrum, which, as we have shown above, causes the appearance of a single peak at c. a. +1 eV with respect to that of pyridinic N (see Fig. 1f). This feature would be simply superimposed on the simulated spectrum of our Ni–CN model (in Fig. 3b), resulting in an increase of the relative intensity of the central peak corresponding to the experimental one at ~399.2 eV.

The local structure of Ni single atoms at the atomic level was further investigated through X-ray absorption spectroscopy (XAS). The X-ray absorption near-edge structure (XANES) data and the corresponding Fourier-transform (FT) extended X-ray absorption fine structure (EXAFS) spectra for two Ni–CN samples with different Ni loading (0.05 and 0.3) are shown in Fig. 4a and b, respectively. The analysis of the XANES region indicated that the oxidation state of Ni is +2 for both Ni–CN samples.[60] The phase-uncorrected FT EXAFS spectra only show one peak at 1.6 Å that can be ascribed to Ni–N and/or Ni–O.[40,59] The absence of peaks in the region between 2.2 Å and 2.8 Å excludes the presence of Ni–Ni and Ni–O–Ni bonds and confirms the atomic dispersion of nickel. Quantitative EXAFS curve fitting analysis (Fig. 4b and Table S3†) was performed to investigate the structural parameters of the Ni–CN samples. For both Ni–CN samples, the best-fitting analysis suggested that Ni atoms had four nearest neighbours at an average distance of 2.06 Å. In the model deduced from our DFT calculations, the Ni atom is stabilized in the large cavity by two pyridinic N atoms and bonds with one of the Cl^- ions. Since such a coordination sphere would not match the experimental evidence, we propose some residual hydration of the Ni sites and included two additional water molecules, along a perpendicular axis to the plane containing the Ni/N atoms. Relaxation of this improved DFT model confirmed it to be a (local) energy minimum. Thus, we decided to refine the fit of the EXAFS spectrum by including two N and two O neighbours. The stabilization of the metal atom by oxygen in the axial position has been previously proposed in the literature.[61,62] The final local structure of the Ni centres deduced by combining the experimental and theoretical data is sketched in Fig. 4c and d (the geometry of the whole model is reported in Fig. S6c†). The two additional optimized water oxygens complete the coordination sphere with Ni–N and N–O distances of 1.98 Å and 2.20 Å, respectively, in very close agreement with the experimental ones (2.02 Å and 2.13 Å), reported in Table S3.†

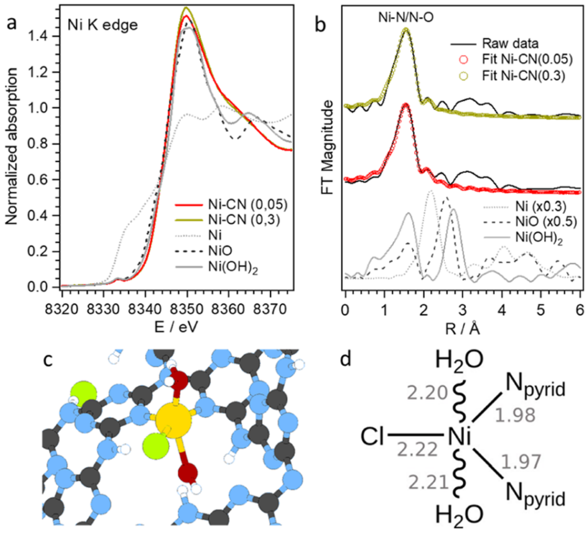

Fig. 4 Local coordination of Ni atoms. (a) XANES region and (b) phase-uncorrected FT EXAFS spectra at the Ni K edge, and the corresponding fit, for Ni–CN(0.05) and Ni–CN(0.2) samples; (c) details of the Ni coordination environment, and (d) corresponding distances in Angstrom. The XANES and FT EXAFS spectra for the samples used as a reference have been included in (a) and (b) for comparison. In panel (c), C, N, H, O, Ni, and Cl atoms are represented by grey, blue, white, red, orange, and green spheres, respectively.

2.2 Electrochemical analysis

The Ni–CN(*X*) samples were tested as OER electrocatalysts. Fig. 5a and b report the LSVs for the Ni–CN samples with different Ni loadings, and the corresponding Tafel plots, respectively. From Fig. 5a, a linear relationship between the Ni content and the catalytic activity is clearly observed for samples with *X* between 0.05 and 0.2, both in terms of current density (J) (Fig. 5c) and onset potential (Fig. 5d). The current density increases with the Ni content, while the onset potential slightly decreases. This confirms that the Ni atoms are the catalytic sites, and that the performance increases with the number of catalytic centers. The generated current was only related to the OER and not to the oxidation of the samples, as proven by rotating ring disk electrode (RRDE) measurements. As observed in Fig. S7,† the increase of the current at both the disk and the ring starts simultaneously, suggesting that the observed currents are only related to the OER. A Tafel slope at around

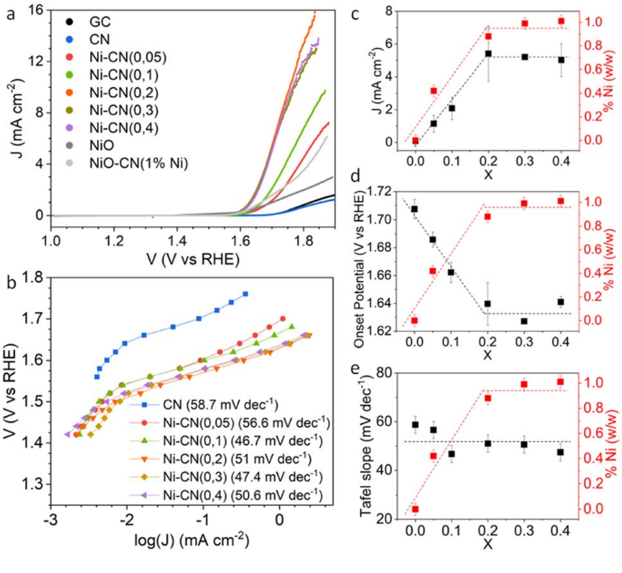

Fig. 5 (a) LSVs (100% iR drop corrected) in O_2-saturated 0.1 M KOH; and (b) corresponding Tafel plots for the Ni–CN(*X*) samples. The LSVs for GC and CN are also included as reference. (c) Current density (J) generated at 1.7 V *vs.* RHE; (d) onset potential; and (e) Tafel slope as a function of Ni content (nominal *X*, and experimental ICP-MS wt%).

50 mV dec^{-1} was obtained for all the Ni-based materials (Fig. 5e), as expected, confirming that all the Ni sites show the same activity, which is independent on the Ni loading. This value suggests that the rate determining step is the deprotonation of the M–*OH centers,[63] and is in accordance with values obtained for carbon matrix stabilized Ni SACs reported in the literature.[30,64,65] The Ni–CN samples with $X \geq 0.2$ showed very similar performance, clearly deduced from the plateau in Fig. 5c–e, which is attributed to the same Ni loading. This means that, even if the Ni precursor : CN ratio is increased during the metalation step, a maximum Ni loading of about 1 wt% can be introduced in the CN matrix, as confirmed by ICP-MS (Table S4†). Fig. 5c–e also report the real Ni loading determined by ICP-MS. This concentration value is much lower than that used in the DFT calculations (8 wt%, corresponding to one Ni atom per supercell including four monomers), but it agrees with the ones reported in the literature for similar materials.[28,57,66,67]

NiO (Sigma-Aldrich) was used as reference and its OER performance was compared with that of the Ni–CN materials (Fig. 5a and b). Two samples were considered: (1) pure NiO (NiO) and (2) a physical mixture of CN and NiO containing 1 wt% Ni (NiO–CN). Both NiO-based samples showed a lower performance than that of the Ni–CN ones, in terms of current density and onset potential. It is interesting to note that NiO–CN performed better than pure NiO, even if the Ni content was lower. This result could be attributed to a better distribution and availability of the Ni centers when they are dispersed in the CN matrix. Comparing the performance of the Ni–CN samples with that reported in the literature for similar materials, we deduced that the Ni–CN samples with $X \geq 0.2$ showed better results. Ohn *et al.* reported a Ni–CN catalyst that gave 1.6 mA cm^{-2} at 1.7 V *vs.* RHE and had a Tafel slope of 60 mV dec^{-1},[30] while the best samples reported in our work gave a current density of 5.4 mA cm^{-2} at the same potential and showed a Tafel slope of 48 mV dec^{-1}. On the other hand, Wu *et al.* reported a current density of 3 mA cm^{-2} at 1.7 V *vs.* RHE and a Tafel slope of 108 mV dec^{-1} for Ni–CN.[68] Xu *et al.* stabilized single Ni atoms in N-doped graphene and obtained a similar current density to those reported in this work, but it should be highlighted that they used a carbon cloth electrode that has higher specific area than glassy carbon (GC) and, therefore, the current densities are not directly comparable. In any case, the Tafel slope that they obtained was 364 mV dec^{-1}, which is much higher than that obtained by our Ni–CN samples.[69]

2.3 Catalytic and structural stability

The stability of the SAC-based catalysts under catalytic conditions is the main issue that hinders their commercial use.[14,15] For this reason, to investigate both the catalytic and structural

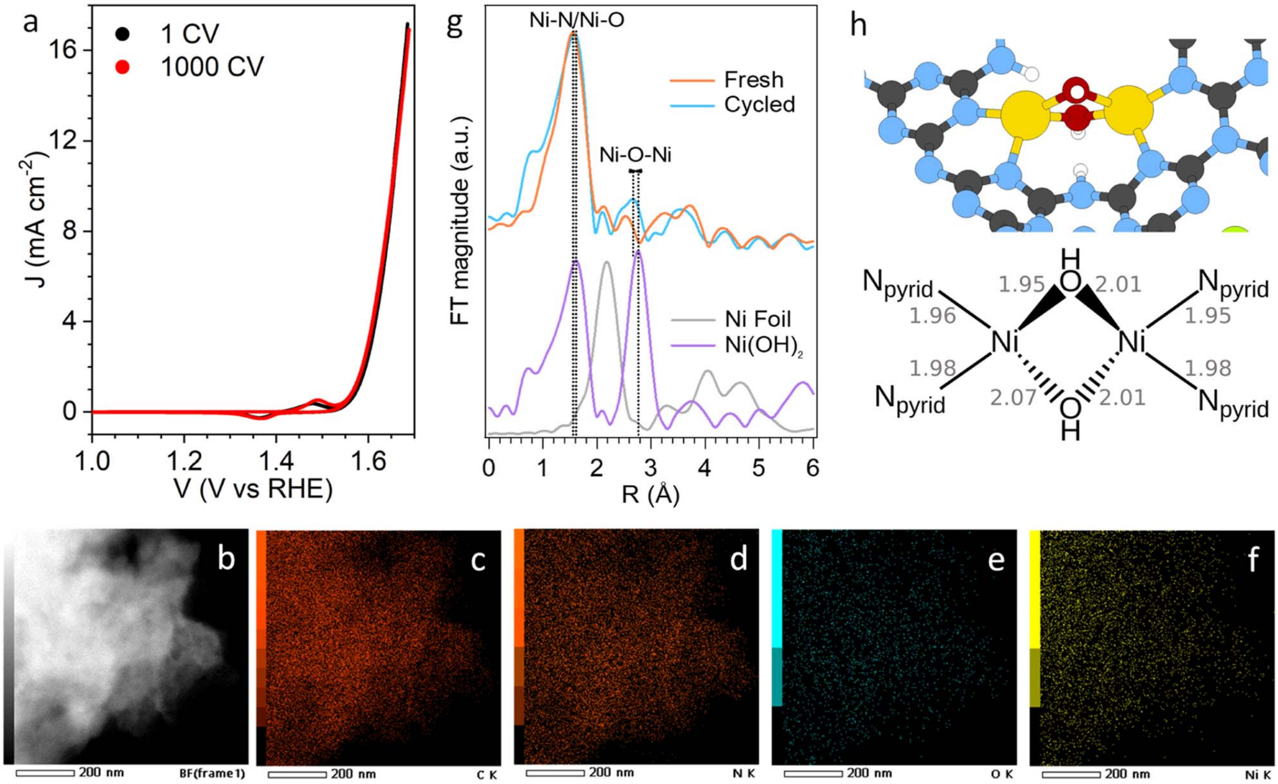

Fig. 6 (a) LSVs (100% iR drop corrected) in O_2-saturated 0.1 M KOH for the pristine and aged Ni–CN(0.2); (b) STEM image of the aged Ni–CN(0.2), and (c)–(f) corresponding elemental mapping images of C, N, O, and Ni; (g) phase shift uncorrected FT EXAFS spectra for aged Ni–CN(0.2); and (h) proposed structure for Ni–CN samples under OER conditions determined from the combination of experimental XAS results and DFT calculations (calculated bond length in Angstrom). The FT EXAFS spectra for the samples used as a reference have been included in (g) for comparison. The EXAFS fits are reported in Fig. S9 and Table S5.†

stability of the Ni–CN based materials, we subjected the Ni–CN(0.2) sample to an accelerated ageing treatment (AAT). After the AAT, the catalytic activity was determined by CV and compared with that of the pristine material, whereas the possible structural changes undergone under catalytic conditions were studied by XAS and HRTEM measurements. Fig. 6a shows the CVs recorded before and after the AAT. As can be observed, both CVs overlap, confirming the good catalytic stability of this material. The morphological and structural stability, on the other hand, were studied by EXAFS and HRTEM. Fig. S8a and S8b† show the HAADF-STEM and BF-STEM images of the aged sample. The images after the ageing treatment are blurry due to the presence of Nafion used in the preparation of the catalytic film. However, the presence of clusters or nanoparticles was not observed. The EDX analysis demonstrated a homogeneous dispersion of C, N, O, and Ni elements, confirming the absence of metal nanoparticles (Fig. 6b–f). Fig. S9a† shows the XANES spectra for the sample before and after the AAT. Both spectra overlap, suggesting that the sample did not suffer significant changes during the cycling treatment. However, to investigate the possible structural changes more in detail, the FT EXAFS spectra were analysed (Fig. 6g). Comparing the phase-uncorrected FT EXAFS spectra for the sample before and after the AAT, a new peak at 2.67 Å appeared in the aged sample, which could be associated with the formation of Ni–O–Ni bonds, similar to those present in $Ni(OH)_2$ (Ni–O–Ni peak at 2.77 Å).[64,70] The appearance of this new peak suggests the partial restructuring of SACs under OER conditions. However, the small intensity of the peak does not suggest the agglomeration of the Ni atoms with the subsequent formation of nanoparticles, in agreement with the HRTEM results.

It is known that the interaction of the single metal atoms and the substrate decreases under catalytic conditions due to the new interactions formed between the metal atoms and the reactant.[16–20] Therefore, under these conditions, the migration of the Ni atoms and the restructuring of the catalyst is facilitated. Taking into account this consideration as well as the HRTEM and XAS post-mortem results, we can hypothesise that the Ni atoms migrate under OER conditions forming Ni–O–Ni bonds similar to those present in Ni LDH, which are considered as the real active sites for the OER.[64] The widening of the peak at around 1.6 Å and the slight shift towards higher distance could be associated with the formation of the new Ni–O–Ni bonds.

Quantitative EXAFS curve fitting analysis was performed to confirm this hypothesis. Results are reported in Fig. S9b, c and Table S5.† The best fitting analysis suggested that Ni atoms had two N neighbours at 1.98 Å, two O neighbours forming the Ni–O–Ni bond at 2.08 Å, and one Ni neighbour at 3.06 Å. This structure agrees with the presence of two Ni atoms in a large cavity, stabilized by two pyridinic N atoms each, and connected between them through two –OH groups like in a Ni LDH structure. To provide additional support to this proposed configuration, we optimized an additional DFT model, where we included two Ni atoms and two –OH groups in a large cavity of the pristine CN (and two additional Cl atoms in two other cavities in order to ensure the charge balance with Ni ions). We find that in the optimized configuration, sketched in Fig. 6h, the four Ni–O (1.95, 2.07, 2.01, and 2.01 Å) and the Ni–Ni distances (3.15 Å) are in good agreement with the experimental values. We highlight that the coordination of the Ni atoms here is tetrahedral, with an average Ni–N distance of 1.96 Å, whereas, in the case of the Ni–CN structure above (Fig. 4c and d), we obtained a distorted bipyramidal trigonal coordination symmetry.

This is one of the few examples of structural stability of SACs under OER conditions in the existing literature. However, our results are in good agreement with those reported by Wan *et al.*, who studied the evolution of single and dual atom Ni/Fe-based electrocatalysts.[64] They performed operando EXAFS and observed a new peak at around 2.78 Å that was attributed to the formation of M–O–M moieties (M = Ni, Fe), similarly to our proposed structure. The preservation of the atomic dispersion was also confirmed by XPS, Raman spectroscopy and HRTEM. On the other hand, Li *et al.* studied single and dual atom Ni/Fe catalysts stabilized in tungsten carbide.[70] They also proposed the reconstruction of WC_x-FeNi catalysts during the OER, with the consequent formation of O-bridged FeNi moieties, by performing EXAFS and HRTEM measurements of the spent catalyst.

3 Experimental section

3.1 Materials synthesis

3.1.1 Pristine CN. Carbon nitride (CN) was obtained through the polymerization of melamine and cyanuric chloride in solution.[46] In detail, 1.27 g (0.01 mol) of melamine and 4.75 g (0.06 mol) of pyridine were dissolved in 50 mL of dimethylformamide (DMF) and put in an ice bath at 0 °C under stirring. Then, a solution of cyanuric chloride (3.58 g, 0.02 mol) in 50 mL of DMF was added dropwise. The final solution was stirred under a nitrogen atmosphere at 0 °C for 6 h and at 25 °C for 12 h, and refluxed at 140 °C for 24 h, in order to control the polymerization process. After cooling down, 150 mL of ethyl acetate were added to precipitate the product that was separated by centrifugation and washed with acetonitrile. Finally, the brown solid obtained was dried under vacuum.

3.1.2 Nickel-decorated CN. Carbon nitride was modified with different amounts of single nickel atoms using $NiCl_2 \cdot 6H_2O$ as a precursor. 100 mg (1 mmol) of CN and the appropriate amount of $NiCl_2 \cdot 6H_2O$ to obtain molar Ni : CN ratios of 0.05, 0.1, 0.2, 0.3 and 0.4 were dissolved in 15 mL of methanol and refluxed at 75 °C for 3 h under a nitrogen atmosphere. After cooling down, 25 mL of acetonitrile were added, and the solution was kept in a close vial at 4 °C for 12 h under static conditions. The material was separated by centrifugation and washed with acetonitrile. Finally, it was dried under vacuum. The materials obtained were labelled as Ni–CN(*X*), with *X* being the molar Ni : CN ratio.

3.2 Physicochemical characterization

TEM images were acquired with an FEI Tecnai G12 microscope. High resolution STEM analyses were performed on a probe Cscorrected Scanning Transmission Electron Microscope, JEOL ARM 200 CF, operated at 80 keV to reduce the impact of the electron beam on the sample. The probe semiconvergence angle was 24 mrad and the HAADF detection angles were set to 68–185 mrad. For chemical analysis a Jeol Centurio EDXS system with a 100 mm^2 SDD detector and Gatan Quantum ER double EELS spectrometer were used.

The X-ray diffraction (XRD) characterization was performed with a Bruker D8 Advance, operating with Cu K$_\alpha$ radiation ($\lambda = 0.15406$ nm) generated at 40 kV and 40 mA.

X-ray photoelectron spectroscopy (XPS) measurements were acquired in a custom-made UHV system working at a base pressure of 10^{-10} mbar, equipped with an Omicron EA125 electron analyser and an X-ray source with a dual Al–Mg anode. Core-level photoemission spectra (C 1s, N 1s, O 1s) were collected at room temperature with a non-monochromatized Al K$_\alpha$ X-ray source (1486.3 eV). Single spectra were acquired using 0.1 eV steps, 0.5 s collection time, and 20 eV pass energy. To analyse the single components of the C 1s and N 1s regions, the spectra were separated into chemically shifted components.

X-ray adsorption spectroscopy (XAS) measurements were recorded on beamline B18 at the Diamond Light Source (UK) with ring energy of 3 GeV and a current of 300 mA. The monochromator used was Si(311) crystals operating in Quick EXAFS (QEXAFS) mode. Pellets of Ni–CN and the oxides used as references were measured in transmission mode at the Ni K (7709 eV) absorption edge at 298 K using a 36-element Ge detector. The Ni foil was measured simultaneously. In addition, a button electrode was prepared by modifying a carbon paper electrode (1 × 1 cm) with the Ni–CN(0.2) sample (Ni loading of 0.023 mg cm^{-2} on the electrode) and subjected to an accelerated ageing treatment (AAT) (1000 cycles between +1.2 and +1.65 V *vs.* RHE at 50 mV s^{-1} in 0.1 M KOH). The cycled electrode was also measured by *ex situ* XAS in fluorescence mode. Calibration of the monochromator was carried out using the Ni foil previously to the measurements. The acquired data were processed and analyzed using the Athena and Artemis programs.

3.3 Electrochemical characterization

Electrochemical measurements were conducted in a three-electrode cell using a Hg/HgO electrode as a reference electrode and a graphite rod as a counter electrode. All the experiments were performed at room temperature. The currents reported are normalized by the electrode geometric area and the potential values are referenced to the reversible hydrogen electrode (RHE). The working electrode consisted of a thin-film catalyst layer deposited on a glassy carbon (GC) electrode (3 mm diameter). Before the catalyst modification, the GC electrode was polished with 0.25 μm diamond paste and sonicated in isopropyl alcohol. The catalyst ink was prepared by mixing 2 mg of catalyst, 500 μl of dimethylformamide (DMF), 500 μl of Milli-Q water and 10 μl Nafion® (5 wt%, Sigma-Aldrich). The ink was sonicated for 40 min to facilitate the dispersion of the catalyst. An aliquot of 20 μl was deposited by drop casting on the GC and dried in air. Linear sweep voltammograms (LSVs) were acquired at 5 mV s^{-1} in O$_2$-saturated 0.1 M KOH, prepared from high purity reagents (Sigma-Aldrich, KOH 99.99%, trace metals basis). The ohmic drop compensation was performed during the data treatment, by using a value for the solution resistance measured by electrochemical impedance spectroscopy (68 Ω for the 0.1 M KOH solution). The error bars were calculated by performing at least two experiments. Tafel slope values were obtained from steady state potential measurements.[71] The steady state polarization curves (Fig. S10†) were constructed by sampling OER current density at the 240th second of chronoamperometry responses acquired at various overpotentials in the catalytic turnover region with a regular interval of 0.020 V. RRDE measurements were performed in a three-electrode cell with the same experimental setup previously described. An aliquot of 7 μl of ink was deposited by drop casting on the GC disk (5 mm diameter). Polarization curves at 1600 rpm were acquired with a scan rate of 5 mV s^{-1} in N$_2$-saturated 0.1 M KOH, prepared from high purity reagents (Sigma-Aldrich). The Pt ring electrode was held at −0.8 V *vs.* Hg/HgO. The AAT was performed as described in section 3.2. In this work, it was not possible to perform more than 1000 cycles since, after that, we observed the partial loss of the catalytic film and, therefore, we were not able to determine the catalytic stability for a higher number of cycles. The optimization of the ink composition in terms of film stability will be studied in future work.

3.4 Computational methods

All our calculations were performed within the DFT framework through the QuantumESPRESSO suite,[72–74] using ultrasoft[75] pseudopotentials with a plane wave basis set of 46 and 326 Ry for the wavefunctions and the charge density, respectively. We relied on pseudopotentials based on the Perdew–Burke–Ernzerhof functional[76] and we included the dispersion forces as a Grimme-D3 correction term.[77] We considered an unshifted Monkhorst-Pack[78] mesh of 4 × 4 × 1 *k*-points, reduced to 2 × 2 × 1 in the case of the models with a 2 × 2 supercell including four monomers. The XRD patterns were constructed by superimposing Gaussian line shapes ($\sigma = 0.02°$) to the structure factors calculated by VESTA software.[79,80] The N 1s XPS spectra were calculated through the ΔSCF scheme,[81] assigning a pseudopotential including a (1s) core-hole to each inequivalent core-excited atom. For these simulations, the plane-wave basis set for the wavefunctions was enlarged to 61 Ry. The core level shifts (CLSs), *i.e.* the change in total energy for every core-excited atom, were convoluted with Gaussian profiles with $\sigma = 0.17$ eV.

4 Conclusions

In this work, we synthesized and carefully characterized carbon nitride nanosheets modified with single Ni atoms by combining experimental and theoretical techniques. Thanks to this approach, we determined that CN has a hexagonal crystal structure with small and large cavities, and that the single Ni atoms are stabilized by two pyridinic N atoms in the large ones. Two additional hydrating water oxygen atoms in the axial position complete the Ni coordination sphere. Subsequently, we tested the Ni–CN materials as OER catalysts under alkaline conditions, observing a linear increase of the activity with the Ni loading, as expected. The catalytic and structural stability of the catalyst were studied by cyclic voltammetry, HR-TEM and XAS post-catalysis measurements. This study showed a good catalytic stability and a partial restructuring of the Ni sites. By combining experimental and theoretical studies, we confirmed the migration of the Ni atoms under OER conditions and the subsequent formation of Ni–O–Ni moieties inside the large cavities of the CN substrate.

Author contributions

N. R. and A. U. investigation, formal analysis, and writing-original draft; C. C. investigation and writing-review; V. C. and G. D. investigation and methodology; C. D. V funding acquisition, supervision, validation, and writing-review and editing; and L. C. conceptualization, funding acquisition, supervision, validation, and writing-review and editing.

Conflicts of interest

The authors declare no conflict of interest.

Acknowledgements

Authors would like to acknowledge support from the Italian Ministry of Education, Universities and Research (MIUR) through the program PRIN 2017–Project no. 2017NYPHN8. C. D. V. acknowledges funding from the European Union – NextGenerationEU through the Italian Ministry of University and Research under PNRR – M4C2I1.4 ICSC – Centro Nazionale di Ricerca in High Performance Computing, Big Data and Quantum Computing (Grant No. CN00000013). L. C. acknowledges funding from the Project Junta de Andalucía - Consejería de Universidad, Investigación e Innovación – Project (P21_00208). N. R. is thankful for support from MIUR and the European Social Fund through the program PON 2014–2020, Project no. DOT1319135-5. G.D. acknowledges the financial support from the Slovenian Research Agency (P2-0421, J2-3041). Dr G. Vilè from the Politecnico di Milano is gratefully acknowledged for the ICP-MS measurements. The authors wish to acknowledge the Diamond Light Source for provision of beamtime (NT28356).

References

1 Y. Jiao, Y. Zheng, M. Jaroniec and S. Z. Qiao, *Chem. Soc. Rev.*, 2015, **44**, 2060–2086.
2 A. R. Zeradjanin, J.-P. Grote, G. Polymeros and K. J. J. Mayrhofer, *Electroanalysis*, 2016, **28**, 2256–2269.
3 M. Tahir, L. Pan, F. Idrees, X. Zhang, L. Wang, J.-J. Zou and Z. L. Wang, *Nano Energy*, 2017, **37**, 136–157.
4 A. Mohammadi and M. Mehrpooya, *Energy*, 2018, **158**, 632–655.
5 M. Bodner, A. Hofer and V. Hacker, *Wiley Interdiscip. Rev. Energy Environ.*, 2015, **4**, 365–381.
6 R. L. Doyle and M. E. G. Lyons, in *Photoelectrochemical Solar Fuel Production*, ed. S. Giménez and J. Bisquert, Springer International Publishing, Cham, 2016, pp. 41–104.
7 E. Bianchetti, D. Perilli and C. Di Valentin, *ACS Catal.*, 2023, **13**, 4811–4823.
8 I. C. Man, H. Su, F. Calle-Vallejo, H. A. Hansen, J. I. Martínez, N. G. Inoglu, J. Kitchin, T. F. Jaramillo, J. K. Nørskov and J. Rossmeisl, *ChemCatChem*, 2011, **3**, 1159–1165.
9 R. Subbaraman, D. Tripkovic, K.-C. Chang, D. Strmcnik, A. P. Paulikas, P. Hirunsit, M. Chan, J. Greeley, V. Stamenkovic and N. M. Markovic, *Nature Mater.*, 2012, **11**, 550–557.
10 T. Kou, S. Wang, J. L. Hauser, M. Chen, S. R. J. Oliver, Y. Ye, J. Guo and Y. Li, *ACS Energy Lett.*, 2019, **4**, 622–628.
11 Y. Cheng, S. Yang, S. P. Jiang and S. Wang, *Small Methods*, 2019, **3**, 1800440.
12 H. Mistry, R. Reske, Z. Zeng, Z.-J. Zhao, J. Greeley, P. Strasser and B. R. Cuenya, *J. Am. Chem. Soc.*, 2014, **136**, 16473–16476.
13 K. Yamamoto, T. Imaoka, W.-J. Chun, O. Enoki, H. Katoh, M. Takenaga and A. Sonoi, *Nature Chem.*, 2009, **1**, 397–402.
14 X.-F. Yang, A. Wang, B. Qiao, J. Li, J. Liu and T. Zhang, *Acc. Chem. Res.*, 2013, **46**, 1740–1748.
15 J. H. Kwak, J. Hu, D. Mei, C.-W. Yi, D. H. Kim, C. H. F. Peden, L. F. Allard and J. Szanyi, *Science*, 2009, **325**, 1670–1673.
16 H.-Y. Zhuo, X. Zhang, J.-X. Liang, Q. Yu, H. Xiao and J. Li, *Chem. Rev.*, 2020, **120**, 12315–12341.
17 K. Rigby and J.-H. Kim, *Curr. Opin. Chem. Eng.*, 2023, **40**, 100921.
18 D. Karapinar, N. T. Huan, N. Ranjbar Sahraie, J. Li, D. Wakerley, N. Touati, S. Zanna, D. Taverna, L. H. Galvão Tizei, A. Zitolo, F. Jaouen, V. Mougel and M. Fontecave, *Angew. Chem., Int. Ed.*, 2019, **58**, 15098–15103.
19 Z. Weng, Y. Wu, M. Wang, J. Jiang, K. Yang, S. Huo, X.-F. Wang, Q. Ma, G. W. Brudvig, V. S. Batista, Y. Liang, Z. Feng and H. Wang, *Nat. Commun.*, 2018, **9**, 415.
20 G. S. Parkinson, Z. Novotny, G. Argentero, M. Schmid, J. Pavelec, R. Kosak, P. Blaha and U. Diebold, *Nature Mater.*, 2013, **12**, 724–728.
21 J. Li, L. Zhang, K. Doyle-Davis, R. Li and X. Sun, *Carbon Energy*, 2020, **2**, 488–520.
22 J. Li, Q. Guan, H. Wu, W. Liu, Y. Lin, Z. Sun, X. Ye, X. Zheng, H. Pan, J. Zhu, S. Chen, W. Zhang, S. Wei and J. Lu, *J. Am. Chem. Soc.*, 2019, **141**, 14515–14519.
23 D. Perilli, D. Selli, H. Liu, E. Bianchetti and C. Di Valentin, *J. Phys. Chem. C*, 2018, **122**, 23610–23622.
24 D. Perilli, D. Selli, H. Liu and C. Di Valentin, *ChemSusChem*, 2019, **12**, 1995–2007.
25 Y. Zheng, Y. Jiao, Y. Zhu, Q. Cai, A. Vasileff, L. H. Li, Y. Han, Y. Chen and S.-Z. Qiao, *J. Am. Chem. Soc.*, 2017, **139**, 3336–3339.
26 X. Li, P. Cui, W. Zhong, J. Li, X. Wang, Z. Wang and J. Jiang, *Chem. Commun.*, 2016, **52**, 13233–13236.
27 S. Sun, G. Shen, J. Jiang, W. Mi, X. Liu, L. Pan, X. Zhang and J. Zou, *Adv. Energy Mater.*, 2019, **9**, 1901505.
28 Y. Li, Y. Wang, C.-L. Dong, Y.-C. Huang, J. Chen, Z. Zhang, F. Meng, Q. Zhang, Y. Huangfu, D. Zhao, L. Gu and S. Shen, *Chem. Sci.*, 2021, **12**, 3633–3643.

29 X. Lv, W. Wei, H. Wang, B. Huang and Y. Dai, *Appl. Catal., B*, 2020, **264**, 118521.

30 S. Ohn, S. Y. Kim, S. K. Mun, J. Oh, Y. J. Sa, S. Park, S. H. Joo, S. J. Kwon and S. Park, *Carbon*, 2017, **124**, 180–187.

31 I. Barlocco, L. A. Cipriano, G. Di Liberto and G. Pacchioni, *Adv. Theory Simul.*, 2022, 2200513.

32 C. Chen, G. Chen and X. Kong, *Inorg. Chem.*, 2018, **57**, 13020–13026.

33 R. Breglia, D. Perilli and C. Di Valentin, *Mater. Today Chem.*, 2023, **33**, 101728.

34 X. Wang, S. Blechert and M. Antonietti, *ACS Catal.*, 2012, **2**, 1596–1606.

35 Y. Wang, X. Wang and M. Antonietti, *Angew. Chem., Int. Ed.*, 2012, **51**, 68–89.

36 G. Vilé, D. Albani, M. Nachtegaal, Z. Chen, D. Dontsova, M. Antonietti, N. López and J. Pérez-Ramírez, *Angew. Chem., Int. Ed.*, 2015, **54**, 11265–11269.

37 Z. Chen, E. Vorobyeva, S. Mitchell, E. Fako, N. López, S. M. Collins, R. K. Leary, P. A. Midgley, R. Hauert and J. Pérez-Ramírez, *Natl. Sci. Rev.*, 2018, **5**, 642–652.

38 X. Wang, S. Qiu, J. Feng, Y. Tong, F. Zhou, Q. Li, L. Song, S. Chen, K. Wu, P. Su, S. Ye, F. Hou, S. X. Dou, H. K. Liu, G. Q. (Max) Lu, C. Sun, J. Liu and J. Liang, *Adv. Mater.*, 2020, **32**, 2004382.

39 Y. Li, B. Li, D. Zhang, L. Cheng and Q. Xiang, *ACS Nano*, 2020, **14**, 10552–10561.

40 J. Feng, H. Gao, L. Zheng, Z. Chen, S. Zeng, C. Jiang, H. Dong, L. Liu, S. Zhang and X. Zhang, *Nat. Commun.*, 2020, **11**, 4341.

41 F. M. Colombari, M. A. R. da Silva, M. S. Homsi, B. R. L. de Souza, M. Araujo, J. L. Francisco, G. T. S. T. da Silva, I. F. Silva, A. F. de Moura and I. F. Teixeira, *Faraday Discuss.*, 2021, **227**, 306–320.

42 W. K. Darkwah and Y. Ao, *Nanoscale Res. Lett.*, 2018, **13**, 388.

43 Q. Hao, G. Jia, W. Wei, A. Vinu, Y. Wang, H. Arandiyan and B.-J. Ni, *Nano Res.*, 2020, **13**, 18–37.

44 X. Li, J. Zhang, L. Shen, Y. Ma, W. Lei, Q. Cui and G. Zou, *Appl. Phys. A*, 2009, **94**, 387–392.

45 P. Niu, L. Zhang, G. Liu and H.-M. Cheng, *Adv. Funct. Mater.*, 2012, **22**, 4763–4770.

46 S. J. Yang, J. H. Cho, G. H. Oh, K. S. Nahm and C. R. Park, *Carbon*, 2009, **47**, 1585–1591.

47 L. Yang, X. Ren, Y. Zhang, Z. Chen and J. Wan, *J. Environ. Chem. Eng.*, 2021, **9**, 105558.

48 J. Gao, Y. Zhou, Z. Li, S. Yan, N. Wang and Z. Zou, *Nanoscale*, 2012, **4**, 3687.

49 F. Fina, S. K. Callear, G. M. Carins and J. T. S. Irvine, *Chem. Mater.*, 2015, **27**, 2612–2618.

50 B. Long, J. Lin and X. Wang, *J. Mater. Chem. A*, 2014, **2**, 2942.

51 Y. Li, H. Zhang, P. Liu, D. Wang, Y. Li and H. Zhao, *Small*, 2013, **9**, 3336–3344.

52 C. Cometto, A. Ugolotti, E. Grazietti, A. Moretto, G. Bottaro, L. Armelao, C. Di Valentin, L. Calvillo and G. Granozzi, *NPJ 2D Mater. Appl.*, 2021, **5**, 63.

53 T. Jia, J. Li, F. Long, F. Fu, J. Zhao, Z. Deng, X. Wang and Y. Zhang, *Crystals*, 2017, **7**, 266.

54 J. Richardson, *Appl. Catal., A*, 2003, **246**, 137–150.

55 S. Deabate, F. Fourgeot and F. Henn, *J. Power Sources*, 2000, **87**, 125–136.

56 D. Vempaire, S. Miraglia, A. Sulpice, L. Ortega, E. K. Hlil, D. Fruchart and J. Pelletier, *J. Magn. Magn. Mater.*, 2004, **272–276**, E843–E844.

57 Y.-Z. Zhang, C. Liang, H.-P. Feng and W. Liu, *Chem. Eng. J.*, 2022, **446**, 137379.

58 X. Zhao, C. Deng, D. Meng, H. Ji, C. Chen, W. Song and J. Zhao, *ACS Catal.*, 2020, **10**, 15178–15185.

59 M. Kwak, J. Bok, B.-H. Lee, J. Kim, Y. Seo, S. Kim, H. Choi, W. Ko, W. Hooch Antink, C. W. Lee, G. H. Yim, H. Seung, C. Park, K.-S. Lee, D.-H. Kim, T. Hyeon and D. Yoo, *Chem. Sci.*, 2022, **13**, 8536–8542.

60 G. Vilé, P. Sharma, M. Nachtegaal, F. Tollini, D. Moscatelli, A. Sroka-Bartnicka, O. Tomanec, M. Petr, J. Filip, I. S. Pieta, R. Zbořil and M. B. Gawande, *Sol. RRL*, 2021, **5**, 2100176.

61 S. Iqbal, B. Safdar, I. Hussain, K. Zhang and C. Chatzichristodoulou, *Adv. Energy Mater.*, 2023, **13**, 2203913.

62 H. Fei, J. Dong, Y. Feng, C. S. Allen, C. Wan, B. Volosskiy, M. Li, Z. Zhao, Y. Wang, H. Sun, P. An, W. Chen, Z. Guo, C. Lee, D. Chen, I. Shakir, M. Liu, T. Hu, Y. Li, A. I. Kirkland, X. Duan and Y. Huang, *Nat. Catal.*, 2018, **1**, 63–72.

63 T. Shinagawa, A. T. Garcia-Esparza and K. Takanabe, *Sci. Rep.*, 2015, **5**, 13801.

64 W. Wan, Y. Zhao, S. Wei, C. A. Triana, J. Li, A. Arcifa, C. S. Allen, R. Cao and G. R. Patzke, *Nat. Commun.*, 2021, **12**, 5589.

65 G. M. Tomboc, T. Kim, S. Jung, H. J. Yoon and K. Lee, *Small*, 2022, **18**, 2105680.

66 T. Jia, D. Meng, R. Duan, H. Ji, H. Sheng, C. Chen, J. Li, W. Song and J. Zhao, *Angew. Chem.*, 2023, **135**, e202216511.

67 Y.-C. Huang, Y. Li, K. T. Arul, T. Ohigashi, T. T. T. Nga, Y.-R. Lu, C.-L. Chen, J.-L. Chen, S. Shen, W.-F. Pong, C.-L. Dong and W.-C. Chou, *ACS Sustainable Chem. Eng.*, 2023, **11**, 5390–5399.

68 C. Wu, X. Zhang, Z. Xia, M. Shu, H. Li, X. Xu, R. Si, A. I. Rykov, J. Wang, S. Yu, S. Wang and G. Sun, *J. Mater. Chem. A*, 2019, **7**, 14001–14010.

69 Y. Xu, W. Zhang, Y. Li, P. Lu and Z.-S. Wu, *J. Energy Chem.*, 2020, **43**, 52–57.

70 S. Li, B. Chen, Y. Wang, M.-Y. Ye, P. A. Van Aken, C. Cheng and A. Thomas, *Nat. Mater.*, 2021, **20**, 1240–1247.

71 S. Anantharaj, S. Noda, M. Driess and P. W. Menezes, *ACS Energy Lett.*, 2021, 1607–1611.

72 P. Giannozzi, S. Baroni, N. Bonini, M. Calandra, R. Car, C. Cavazzoni, D. Ceresoli, G. L. Chiarotti, M. Cococcioni, I. Dabo, A. Dal Corso, S. De Gironcoli, S. Fabris, G. Fratesi, R. Gebauer, U. Gerstmann, C. Gougoussis, A. Kokalj, M. Lazzeri, L. Martin-Samos, N. Marzari, F. Mauri, R. Mazzarello, S. Paolini, A. Pasquarello, L. Paulatto, C. Sbraccia, S. Scandolo, G. Sclauzero, A. P. Seitsonen, A. Smogunov, P. Umari and R. M. Wentzcovitch, *J. Phys.: Condens. Matter*, 2009, **21**, 395502.

73 P. Giannozzi, O. Andreussi, T. Brumme, O. Bunau, M. Buongiorno Nardelli, M. Calandra, R. Car, C. Cavazzoni, D. Ceresoli, M. Cococcioni, N. Colonna, I. Carnimeo, A. Dal Corso, S. De Gironcoli, P. Delugas, R. A. DiStasio, A. Ferretti, A. Floris, G. Fratesi, G. Fugallo, R. Gebauer, U. Gerstmann, F. Giustino, T. Gorni, J. Jia, M. Kawamura, H.-Y. Ko, A. Kokalj, E. Küçükbenli, M. Lazzeri, M. Marsili, N. Marzari, F. Mauri, N. L. Nguyen, H.-V. Nguyen, A. Otero-de-la-Roza, L. Paulatto, S. Poncé, D. Rocca, R. Sabatini, B. Santra, M. Schlipf, A. P. Seitsonen, A. Smogunov, I. Timrov, T. Thonhauser, P. Umari, N. Vast, X. Wu and S. Baroni, *J. Phys.: Condens. Matter*, 2017, **29**, 465901.

74 P. Giannozzi, O. Baseggio, P. Bonfà, D. Brunato, R. Car, I. Carnimeo, C. Cavazzoni, S. De Gironcoli, P. Delugas, F. Ferrari Ruffino, A. Ferretti, N. Marzari, I. Timrov, A. Urru and S. Baroni, *J. Chem. Phys.*, 2020, **152**, 154105.

75 D. Vanderbilt, *Phys. Rev. B*, 1990, **41**, 7892–7895.

76 J. P. Perdew, K. Burke and M. Ernzerhof, *Phys. Rev. Lett.*, 1996, **77**, 3865–3868.

77 S. Grimme, J. Antony, S. Ehrlich and H. Krieg, *J. Chem. Phys.*, 2010, **132**, 154104.

78 H. J. Monkhorst and J. D. Pack, *Phys. Rev. B*, 1976, **13**, 5188–5192.

79 K. Momma and F. Izumi, *J. Appl. Crystallogr.*, 2011, **44**, 1272–1276.

80 F. Izumi and K. Momma, *SSP*, 2007, **130**, 15–20.

81 S. García-Gil, A. García and P. Ordejón, *Eur. Phys. J. B*, 2012, **85**, 239.